Hydrazine selective decomposition over metal free carbonaceous materials

Ilaria Barlocco[a], Silvio Bellomi[a], Simone Tumiati[c], Nikolaos Dimitratos[d], Alberto Roldan*[b], Patrizia Fumagalli[c], Alberto Villa*[a]

[a] Dipartimento di Chimica, Università degli Studi di Milano, via Golgi 19, I-20133Milano, Italy

[b] Cardiff Catalysis Institute, School of Chemistry, Cardiff University, Main Building, Park Place, CF10 3AT, Cardiff, United Kingdom

[c] Dipartimento di Scienze della Terra "Ardito Desio", Università degli Studi di Milano, via Mangiagalli 34, I-20133 Milano, Italy

[d] Dipartimento di Chimica Industriale e dei Materiali, ALMA MATER STUDIORUM Università di Bologna, Viale Risorgimento 4, 40136 Bologna, Italy

*Corresponding authors

E-mail addresses: Alberto.Villa@unimi.it (A. Villa), RoldanMartinezA@cardiff.ac.uk (A. Roldan)

Abstract

Herein we report a combined experimental and computational investigation unravelling the hydrazine hydrate decomposition reaction on metal-free catalysts. The study focuses on commercial graphite and two different carbon nanofibers, Pyrolytically Stripped (CNF-PS) and High Heat-Treated (CNF-HHT), respectively treated at 700 and 3000 °C to increase their intrinsic defects. Raman spectroscopy demonstrated a correlation between the initial catalytic activity and the intrinsic defectiveness of the carbonaceous materials. The CNFs-PS higher defectivity (I_D/I_G = 1.54) leads to the most performing metal-free catalyst, showing a hydrazine conversion of 94% after 6 hours of reaction and a selectivity to H_2 of the 89%. In addition, to unveil the role of NaOH CNFs-PS were also tested in absence of alkaline solution, showing a decreasing in the reaction rate. Density functional theory (DFT) demonstrated that the single vacancies (SV) present on the graphitic layer is the only active site promoting the hydrazine decomposition, whereas other defects such as double vacancy (DV) and Stone-Wales defects (SW) are unable to adsorb hydrazine fragments. Two symmetrical and one asymmetrical dehydrogenation pathways were found, in addition to an incomplete decomposition pathway forming N_2 and NH_3. On the most stable hydrogen production pathway, the effect of the alkaline medium was elucidated through calculations concerning the diffusion and recombination of atomic hydrogen. Indeed, the presence of NaOH helps extracting H species without additional energetic barriers, as opposed to the calculations performed in polarizable continuum medium. Considering the initial hydrazine dissociative adsorption, the first step of the dehydrogenation pathway is the more favourable than the scission of the N-N bond, which lead to NH_3 as product. This first reaction step is crucial to define the reaction mechanisms and the computational results are in agreement with the experimental ones. Moreover, comparing two different hydrogen production pathways (with and without diffusion and recombination), we confirmed that the presence of sodium hydroxide in the experimental reaction environment can modify the energy gap between the two pathways, leading to an increased reaction rate and selectivity to H_2.
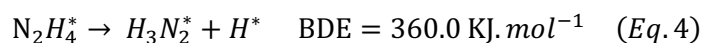
Introduction

Green and sustainable sources of energy are essential to mitigate the environmental impact of fossil fuels and the rising energy demand. Hydrogen have been recognised as one of the most suitable alternative energy vectors due to its high energy and innocuous products upon utilisation [1]. Even though its benefits, hydrogen direct usage is inhibited by the scarcity of economically and safe hydrogen storage technologies [2]. Hence, alternative approaches to store and transport it [3–6], and materials that release hydrogen under mild condition, are urgently required [7].

Hydrazine (N_2H_4) can be employed as hydrogen carrier because it is liquid at T < 114 °C (1 atm) and can be easily transported [8–11]. In addition, it is a carbon-free fuel, hence avoiding undesired emissions, e.g. CO_2, and species damaging the catalysts as seen in CO poisoning Pt/C electrodes in proton exchange membrane fuel cells (PEMFCs) [12,13]. Currently, the N_2H_4 exothermic decomposition is employed as a propellant in aerospace application, i.e., in rockets and artificial satellites [14,15]. N_2H_4 possesses an hydrogen content of 12.5 wt% [16] and decomposes into a mixture of ammonia, hydrogen and nitrogen in the presence of catalysts such as Shell 405 (30 wt % Ir/Al_2O_3) [17,18]. N_2H_4 decomposition occurs into two different pathways [19–21]:

$$N_2H_4 \rightarrow N_2(g) + 2H_2\,(g) \quad \Delta H = -95.4 \text{ KJ. mol}^{-1} \quad (Eq.\,1)$$

$$3N_2H_4 \rightarrow N_2(g) + 4NH_3\,(g) \quad \Delta H = -157.0 \text{ KJ. mol}^{-1} \quad (Eq.\,2)$$

The first reaction (Eq. 1) represents the complete reforming pathway, where molecular hydrogen and nitrogen are produced. The second reaction (Eq. 2) is thermodynamically favoured and produces ammonia and nitrogen. The selectivity of the reaction can vary with the reaction conditions, such as pressure, temperature and catalyst presence [22–25]. In a typical hydrazine catalytic decomposition process on metal surfaces, the molecule adsorbs on catalyst surface (below marked with and asterisk) driving the N-N or the N-H cleavage. From a thermodynamic point of view, the cleavage of the N-N bond (Eq. 3) is favoured compared to the N-H bond dissociation energy (BDE, Eq. 4) [26,27] Hence, the nature of the catalyst plays a crucial role in quenching the incomplete decomposition pathway (Eq. 2) and promoting the cleavage of N-H bond (Eq. 4).

$$N_2H_4^* \rightarrow H_2N^* + H_2N^* \quad BDE = 286.0 \text{ KJ. mol}^{-1} \quad (Eq.\,3)$$

$$N_2H_4^* \rightarrow H_3N_2^* + H^* \quad BDE = 360.0 \text{ KJ. mol}^{-1} \quad (Eq.\,4)$$

Because of its hypergolic nature, the risk of explosion is one of the most serious problem related to handling hydrazine, especially in the presence of a metal that may catalyse its decomposition [28]. One solution can be the dilution of N_2H_4 in inert gas such as argon [25] or in water, forming hydrous hydrazine ($N_2H_4 \cdot H_2O$), which can be particularly important as a liquid hydrogen source [29]. Hydrous hydrazine still contains 7.9 wt % of hydrogen, avoiding all the issues related to H_2 storage and transportation [7,30]. The development of a catalyst capable to exothermically react with $N_2H_4 \cdot H_2O$ and selectively decompose it into hydrogen is key for a H_2-based economy [26,31]. In order to generate hydrogen in a controlled manner and on-demand, different supported [32–34] and unsupported metal NPs have been investigated [13,15,28]. At first, noble metals such as Ir [29,35] and Rh [10,36] performed well as reforming catalyst. Nevertheless, due to the cost and synergetic catalytic properties, Ni was introduced as second metal providing superior activity and selectivity [33,37–43].

The presence of NaOH in the hydrazine decomposition environment can favour its selective decomposition, suppressing the formation of NH_3. In particular, Wang et al. have demonstrated that adding a 0.5 M solution of NaOH to unsupported Ni nanoparticles (NPs) can enhance the selectivity to H_2 from 64 % to 100 % [44]. In addition, Peng and co-workers have performed theoretical and experimental studies on Pt-Ni/C catalysts showing a strong dependence of the selectivity and reaction rate with the pH [45]. Indeed, the presence of OH^- facilitates the N-H scission and promotes the H_2 and H_2O formation [11,46].

Despite the excellent activity, selectivity and stability of metal-based catalysts [27,47–51], employing metals is raising reservations about the overall sustainability of hydrogen production reactions [52–54]. On the other hand, in the last few decades, carbon-based catalysts are attracting significant attention on replacing metal-based materials in heterogeneous catalysis. Different studies have demonstrated that metal-free carbon materials can be effective in gas phase reactions, in particular for alkenes and alkanes dehydrogenation [55–57], and in liquid phase reactions, i.e., oxidation of benzene [58] and alcohols [59,60], and reductions such as acetylene, carbon-carbon multiple bonds and functionalized benzenes [61,62].

Combining experimental and DFT studies, we reported the activity of metal-free carbon catalysts in the generation of H_2 from formic acid [63]. In particular, we demonstrated that defects, especially single vacancies, are active in the formic acid dehydrogenation reaction even in the presence of oxygen groups, i.e., alcohols and carbonyls. Similar investigations including a wide range of carbon dopants proved the same results on ammonia reforming [64]. For the best of our knowledge, the decomposition of hydrazine on a metal-free carbon-based catalyst has been reported only on $g-Si_3C$, which is able to adsorb N_2H_4 in its *anti*-configuration and decompose it following pathways different to those on metal surfaces [65].

In the present work, different carbonaceous materials, i.e., graphite and two different types of carbon nanofibers differing in graphitization degree (PR24-PS and PR24-HHT), were employed in the liquid phase hydrazine decomposition reaction. A systematic density functional theory (DFT) study on N_2H_4 adsorption and decomposition was employed to understand the role of the defects in this process, paving the pathway to the development of new and efficient carbo-catalysts.

EXPERIMENTAL METHOD

Materials and chemicals: CNFs PR24-PS and PR24-HHT were purchased from the Applied Science Company. These nanofibers were prepared with different post-treatment temperature, in order to remove polyaromatic carbon layers covering their external surface. The thermal treatments were performed at 700 and 3000 °C for PR24-PS and PR24-HHT, respectively. Graphite was obtained from Johnson Matthey. $N_2H_4 \cdot H_2O$ (98 %), sodium hydroxide (NaOH, ≥98 %), hydrochloric acid (HCl, 37 % wt) and 4-dimethylaminobenzaldehyde (4-DMAB, 98 %) were acquired from Sigma-Aldrich.

Catalytic tests: Liquid phase $NH_2NH_2 \cdot H_2O$ decomposition was performed at a constant reaction temperature of 50 °C using a 50 mL three-necked round bottom flask, with one of the flask's neck connected with a burette employed for gas volume analyses.

Typically, the required amount of catalyst (hydrous hydrazine/catalyst weight ratio 15.7/1) was added in the reactor, where 16.0 mL of a 0.5 M NaOH aqueous solution was placed and heated at the desired temperature. Once the solution reached the desired temperature, 600 µL of a 3.3 M hydrous hydrazine aqueous solution was inserted and the final mixture was stirred at 1400 rpm using a magnetic stirrer.

Product analyses: Hydrous hydrazine conversion was analysed using a Jasco V-730 Spectrophotometer, using a 1 cm quartz cell. The conversion was calculated according to the equation $mol_{in} - mol_{out}/ (mol_{in} \times 100)$,

where mol$_{in}$ and mol$_{out}$ are the initial and the remaining moles, respectively. The analytical method was based on the reaction of $N_2H_4 \cdot H_2O$ with 4-dimethylaminobenzaldehyde (4-DMAB) in dilute hydrochloric acid (Scheme 1). The substrate quantitatively reacts with 4-DMAB to give a p-quinone structure that adsorb at 456 nm [66,67]. The concentration was calculated using the Beer-Lambert equation.
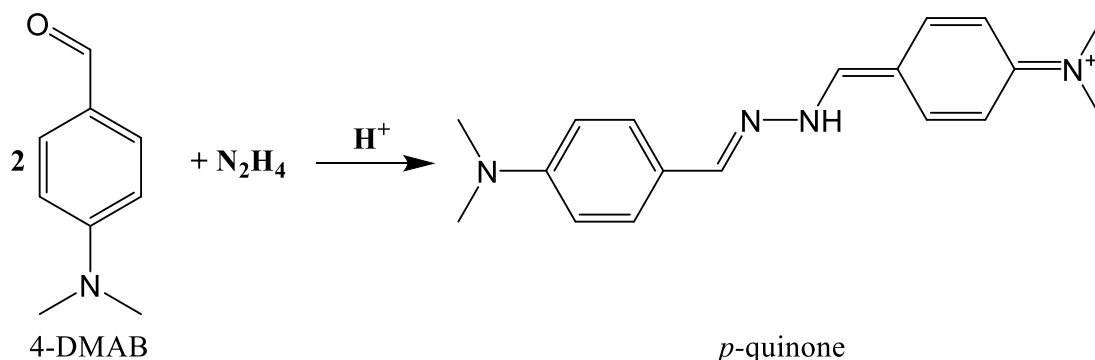
Scheme 1: Reaction of 4-DMAB and hydrazine to give the yellow p-quinone

The volume of gas produced was measured using the water displacement method. The gaseous products released were allowed to pass to a trap containing a 0.05 M HCl aqueous solution to ensure the removal of NH$_3$, if any, and volumetrically monitored employing the burette. Using this method, the volume measured was only due to N$_2$ and H$_2$ molecules, enabling us to evaluate n(N$_2$+H$_2$). The selectivity to hydrogen (x) was then calculated according to Eq. 5:

$$3NH_2NH_2 \rightarrow (1 + 2x)\,N_2 \; + \; 6x\,H_2 \; + \; 4(1 - x)\,NH_3 \tag{Eq.5}$$
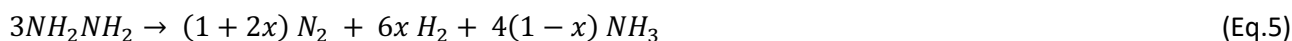
Considering the molar ratio n(N$_2$+H$_2$) / n(N$_2$H$_4$) (λ), x can be evaluated as Eq. 6:

$$x = \frac{3\lambda - 1}{8} \tag{Eq.6}$$

Catalyst characterization: Carbon samples were characterized by ICP-OES and Raman spectroscopy.

Raman spectroscopy was executed using a Horiba LabRam HR Evolution micro-Raman spectrometer equipped with a green solid-state laser (532 nm) focused through a 100× objective, giving a spatial resolution of approximately 1 μm. The micro-Raman system was set with 300 lines per mm grating; the spectrum was collected with a final laser power of about 0.1 mWat. The sample surface was measured through a hand-held power meter. Spectra were calibrated using the 520.7 cm−1 line of a silicon wafer. The sample was scanned at an attenuation time of 300 s and 2 scans were performed giving a spectrum.

The presence of possible residual metal was analysed by inductively coupled plasma optical emission spectroscopy (ICP-OES) using a PerkinElmer Optima 8000 emission spectrometer.

Computational method: Periodic plane-wave density functional theory (DFT) calculations were carried out using the Vienna Ab-initio Simulation Package (VASP) [68,69]. The generalized gradient approximation from the revised Perdew-Burke-Ernzerhof approximation (RPBE) [70] has been used to take into account the correlation-exchange electronic contributions, with a kinetic energy cutoff of 500 eV chosen for the expansion of the Kohn–Sham valence states plane-waves [71]. All the calculations includes the long-range dispersion correction approach by Grimme – DFT-D3 methods [72,73], an improvement on pure DFT to evaluate molecular interactions[74–77]. We also included the implicit solvation model as implemented in VASPsol [78,79], where solvent is considered as a polarizable continuum dielectric bath. The optimization thresholds for electronic and ionic forces relaxation were respectively 10^{-5} eV and 0.02 eV/Å. For Brillouin

zone sampling, a Γ-centered k-point mesh generated through Monkhorst–Pack method of dimensions 5 × 5 × 1 in order to avoid Pulay stress [80]. To improve the convergence of the Brillouin-zone, a first order Methfessel–Paxton method has been used with an energetic width value of 0.2 eV. All carbon-based materials were modeled starting from a single layer slab of a 6 x 6 pristine graphene supercell and introduced different defects: single vacancy (SV), double vacancy (DV) and three different Stone Wales defects (SW1, SW2, SW3) [63]. The supercell is in a hexagonal crystalline system with unit cell vectors *a* and *b* lying in surface plane and perpendicular to *c* axis. Both, *a* and *b,* were optimized at 14.8 Å, in well agreement with experimental values obtained by Transmission Electron Aberration-corrected Microscope (TEAM) [81]. We introduced a polarizable continuum dielectric bath of ~16 Å perpendicular to the C-surface in order to avoid spurious periodic interactions with periodic images. Computational characterization of the surfaces was performed using the Bader analysis as implemented by Henkelmann et al. [82]. A fast convergence of charges with respect to the Fast Fourier Transform grid was obtained employing the Grid Method by Yu [83], which quadratically converges charge values with respect to mesh size. A grid of 370 x 370 x 390 points was applied in order to optimize memory usage and precision of the calculations. These values were obtained converging two equivalent carbon charges in pristine graphene. Charge density local curvatures, local accumulations and depletions were evaluated to disclose the ability of every inequivalent surface site to adsorb and decompose hydrazine. The optimized parameters obtained from the Grid method were employed in a Laplacian topological analysis [84]. The AIM-UC Bader Analysis Toolkit implemented by David Vega et al. [85] was applied on a total electron density obtained combining the valence charge data and the core charges, resulting in Laplacian of charge density map, which allowed to analyze Bond Critical Points (BCP). Before adsorbing the hydrazine molecule, a systematic study on all possible active sites was performed using NH_3 as a probe molecule and considering both dissociative and non-dissociative adsorption modes. The molecular adsorption energy (E_{ADS}) was defined as the difference between the combined system and the isolated species. The reaction energy (E_R) of each N_2H_4 dissociation elementary step was described as the total energy difference between the final (final adsorbate/C) and the initial states (initial adsorbate/C). Hydrogen diffusion calculations were performed on the single vacancy (SV) system, which proved to be the most active defect in this study. A hydrogen atom was placed in the desired position where only its *z* coordinate could relax during the optimization calculation. Later on, all carbon atoms were allowed to relax except two of them sufficiently far from the active site to avoid rotations or translations of the considered surface as a whole [86]. The hydrogen diffusion energy (E_D) was calculated as the energy difference between atomic hydrogen within the vacancy, in the most stable configuration, and diffused atomic hydrogen structures.

RESULTS

Different carbonaceous materials, i.e., CNFs-PS, CNFs-HHT and graphite were employed as catalysts for the hydrous hydrazine reforming reaction. ICP-OES analysis was employed to ensure the absence of possible metallic impurities. The reaction conditions were optimized to assess the reaction kinetic regime and to establish the correct amount of catalyst to be used. The optimum conditions were at 50 °C and 1400 rpm, using 600 μL of a hydrazine solution 3.3 M in 16 mL of NaOH 0.5 M and a $N_2H_4 \cdot H_2O$:catalyst weight ratio of 15.7:1. To ensure reproducibility, all the experiments were repeated three times. Figure 1 shows the different kinetic profiles for 6 h of reaction. CNFs-PS exhibited the highest conversion at 6 h (94 %), whereas CNFs-HHT and graphite showed similar conversion (71 % and 65 %, respectively) (Table 1, column 4). On the most active material, CNFs-PS, H_2 selectivity was calculated using water displacement method and 89 % selectivity for the complete hydrazine decomposition reaction was determined.
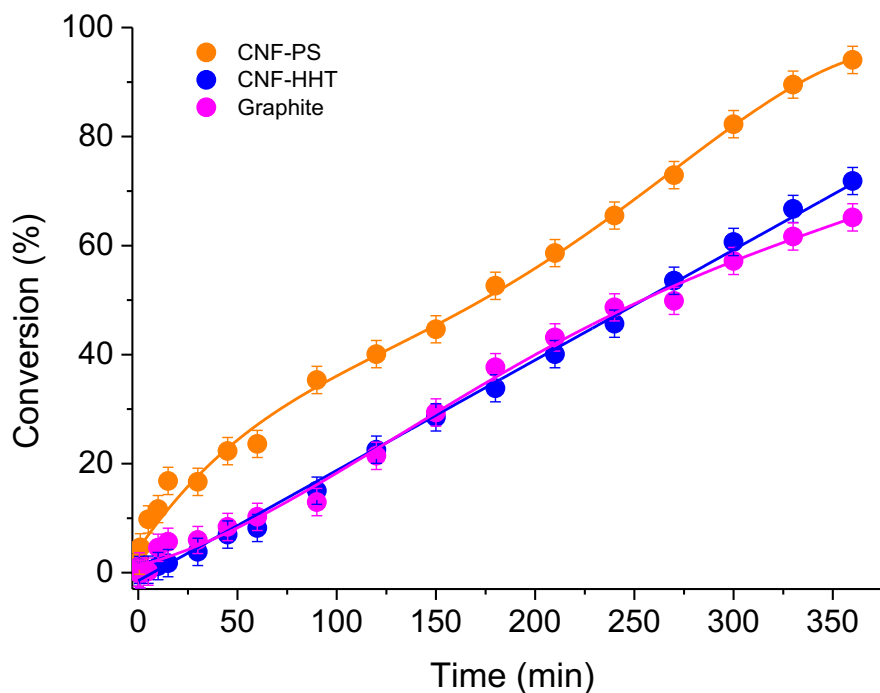
Figure 1 Conversion trend for the hydrazine decomposition reaction for the different carbonaceous materials: Graphite (violet), CNFs PR24-PS (orange) and PR24-HHT (blue). All the tests were performed at 50 °C and 1400 rpm, using 600 µL of a hydrazine solution 3.3 M in 16 mL of NaOH 0.5 M and a $N_2H_4 \cdot H_2O$:catalyst weight ratio of 15.7:1.

In order to rationalize these results in terms of structural properties, we characterized all the catalysts using Raman spectroscopy. It allowed us to investigate the graphitization degree of carbon materials measuring the two bands at around 1600 cm^{-1} (G band) and 1350 cm^{-1} (D band) [87]. The G band is generated by the C=C stretching vibrations in the graphite lattice, and it is related to structurally ordered graphite domains. The D band corresponds to the A_{1g} mode, which is forbidden according to the selection rules in graphite, but active in the presence of structural defects or in plane substitutional heteroatoms [87]. All carbon materials studied in this work present both D and G Raman bands with the following I_D/I_G ratio: CNF-PS (1.54) > Graphite (0.20) > CNFs-HHT (0.11) (Figure S1 and Table 1).

Table 1: Raman characteristics of the carbon catalyst, their initial catalytic activity (15 minutes of reaction) and final conversion towards hydrazine decomposition (6 h).

	Raman I_D/I_G	Activity at 15 min (mg^{-1}min^{-1}) *10^2	Conversion at 6 h (%)
Graphite	0.20	6.0	65
CNFs-PS	1.54	18	94
CNFs-HHT	0.11	1.9	71

To unveil the effect of NaOH in the reaction environment, the most active material (i.e. CNFs-PS) was tested at the same experimental conditions, but with distilled water as solvent, i.e. pH=7. From the comparison between the reaction profiles showed in Figure 2, it appears clear that the presence of NaOH affects not only the selectivity of the reaction, but also its kinetics [11,46]. Indeed, the catalyst tested at the same conditions with NaOH exhibited about 70% of hydrous hydrazine conversion at 4 h of reaction, while the same material tested in water presented a 15 % conversion.
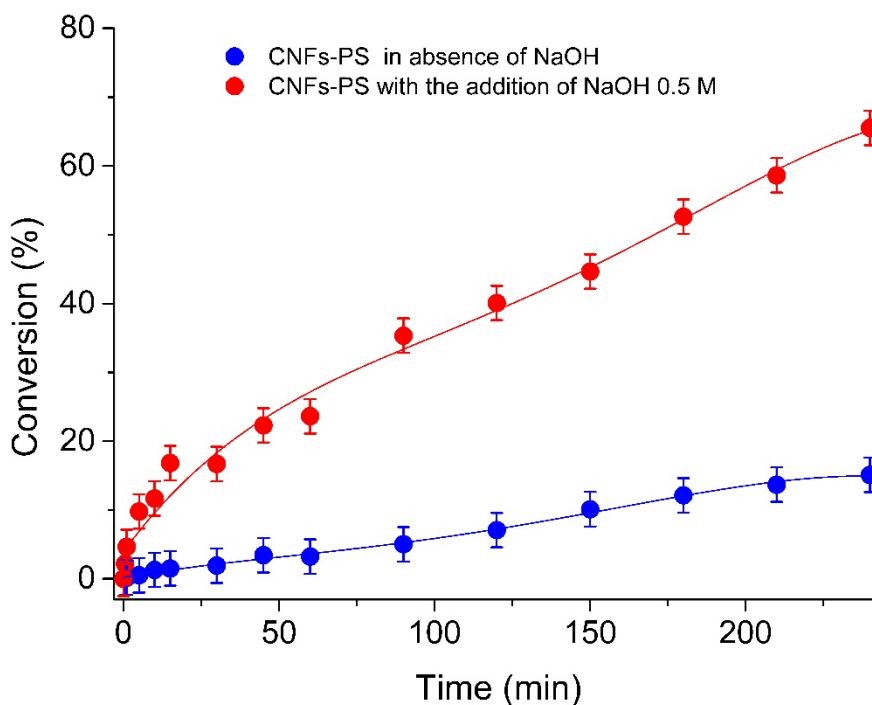
Figure 2 Comparison of conversion trend for hydrazine decomposition in a different reaction environment. Alkaline aqueous solvent, red solid line, and distilled water, blue solid line. All the tests were performed at 50 °C and 1400 rpm, using 600 µL of a hydrazine solution 3.3 M in 16 mL of solvent (NaOH 0.5 M for red profile, distilled water for the blue one) and a $N_2H_4 \cdot H_2O$:catalyst weight ratio of 15.7:1.

Systematic DFT simulations were performed to elucidate the roles of carbon defects in hydrazine activation and decomposition. Six different graphitic surfaces were modelled: pristine graphite (PG), single vacancy (SV), double vacancy (DV) and three different Stone-Wales defects (SW, VSW1, VSW2), represented in Figure S1. Prior to proceed with the adsorptions, we performed an evaluation of charge density at Bond Critical Points (BCP)[88] to estimate the potential active sites of the different optimized surfaces (Figure S1). As previously shown, only sites presenting distortions in the graphene π-system are able to interact favourably with adsorbates [64]. The obtained electron densities measured on the defects are summarised in Table 2. It was observed that only SV and DV are potential catalysts candidates to bind N_2H_4 as these two structures contain dangling C-atoms lacking electron density [63]. This result, underling the localization of the catalytic site on both SV and DV.

Table 2: Charge density at Bond Critical Points of the potential active sites.

Surface Site	$\rho(\vec{r}_{BCP}) \; / \; \frac{e^-}{Å^3}$
PG	2.03
SV	0.587
DV	0.974 and 0.979
SW	1.863 - 2.589

VSW1	1.628 - 2.156
VSW2	1.602 - 2.134

We validated the assumptions regarding the active sites by using ammonia (NH_3) as a probe molecule. It was brought near non-equivalent active sites and the system relaxed. In line with previous studies, the graphitic areas possess an inactive π-conjugation, not sensitive to adsorption of molecules [64,89–91]. Only single vacancies showed a favourable (exothermic) interaction with ammonia, indicating that a $\rho(\vec{r}_{BCP})$ smaller than 0.6 $\frac{e^-}{\text{Å}^3}$ defines the active sites on carbon surfaces. Combining the Laplacian of charge density analysis and the performed tests with NH_3, we were able to identify C_3, $C_{3'}$ and C_7 in the single vacancy system as possible active sites (Figure 3). Then, hydrazine was placed and relaxed on such sites with different initial orientations. We also investigated the molecule dissociative adsorption [92,93], i.e., breaking the N-H or N-N bonds while forming a new one with the surface similar to previous works on metal surfaces.
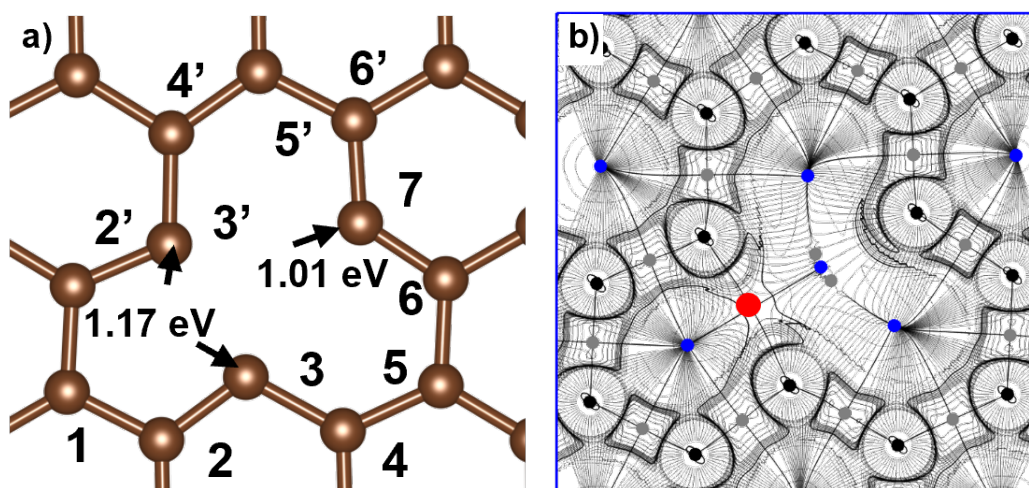

Figure 3 Single vacancy representation. a) Individuated active sites and NH_3 relative adsorption energies. b) Charge-density Laplacian analysis iso-surfaces plot; Red circle indicates the evaluation site for $\rho(\vec{r}_{BCP})$, black circles indicate nuclear charge density maxima, grey Bond Critical Points and blue Ring Critical Points.

The least stable N_2H_4 adsorption configuration is the anti-single linked (*a-SL*) configuration where hydrazine bonded C_3 (Figure 4a). When the molecule is bonded to two active sites in a bridge configuration, it may adopts the cis-bridged (*cB-N*) configuration driving the N-H dissociation (Figure 4b) or the cis-bridged (*cB-H*) structure resulting in the N-N bond scission (Figure 4c). It can be seen from the adsorption energies inserted in Figure 4 that the resulting stability increases following the sequence a-SL < cB-N < cB-H. Zheng et al. investigated the same adsorption process on metal-free SiC_3 siligraphene resulting in the following stability sequence: cis-N_2H_4 < gauche-N_2H_4 < anti-N_2H_4 [65]. In addition, mechanistic studies performed on metal surfaces, such as Ir [94], Cu [95], Ni [96–98] and Pt [99], are consistent with the siligraphene trends. In our study, a gauche adsorbed configuration was not obtained from structural optimizations, which shows C behaves differently to SiC_3 siligraphene and metals. Unlike in these studies, the different adsorption modes on defective graphene are driven by the lack of electron density. Hence, the *a-SL* structure only saturates one dangling carbon atom showing a week adsorption energy (E_{ADS} = -0.78 eV), whereas when two or more

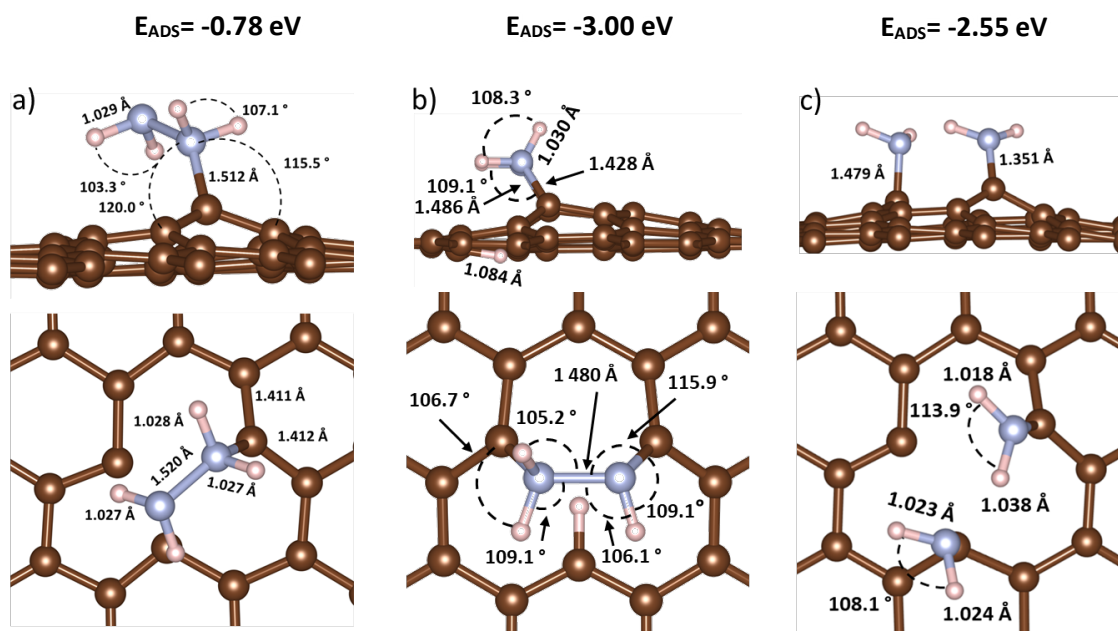dangling bonds are saturated (cB-N and cB-H, respectively), the species are more strongly bonded to the surface.

Figure 4: Top and side view of the most favourable Hydrazine configurations: a) a-SL b) cB-N c) cB-H. Inset are the adsorption energies (E_{ADS}) and the main distances (Å) and angles (°) of interest. Carbon atom is labelled in brown, nitrogen in blue and hydrogen in white.

We considered two symmetric and one asymmetric dehydrogenations, and incomplete decomposition pathways based on previous reports [19–21]. However, only the most stable routes to the formation of H_2 and NH_3 was analysed in detail. The cB-H was the most stable adsorption configuration and the first step for the complete hydrazine reforming (Eq. 1), whereas the cB-N was the first step towards an incomplete hydrazine decomposition (Eq. 2) (Figure 4b and c). The difference in energy between the N-H and the N-N dissociative adsorptions indicated that the hydrogen production pathway was the preferable one ($\Delta E_{(NN-NH)}$ = 0.450 eV). Indeed, once the N-H bond was broken and a C_3-H was formed leading towards the hydrogen production.

To proceed with dehydrogenation reaction mechanisms, we could consider a negligible activation energy for the migration of the dissociated H adatoms similar to the spill on metal catalysts [100]. However, the SV is a point defect, and the active site is isolated from adjacent dangling bonds. Thus, two different hydrogen production pathways were tested (Figure 5). The first one, SWC-Decomposition (Symmetric non-directional solvent Complete decomposition, Figure 5), simulated the absence of an alkaline aqueous medium and the H species needed to overcome a non-negligible diffusion energy barrier to free the active site. Hence, we investigated the H migration along three different paths (Figure S3) in similar fashion to previous studies [101–103]. For the most favourable migration pathway (Figure S4), we obtained a diffusion energy barrier of (E_D) 3.48 eV in polarizable continuum background, which did not provide a realistic directional solvation in aqueous solutions [102] (Figure S5). According to our simulations, two H atoms occupying nearest neighbour dangling carbon sites had an endothermic reaction energy (E_R = 2.90 eV) to form H_2 (Figure S6). However, the experiments were performed in solution, which surrounded H* with an arranged (dipole) solvation shell promoting the H diffusion through the solution as well as the H_2 evolution through the Heyrovsky mechanism [104]. Thus, we considered the desorption from C_3 (Figure 3) negligible in comparison with the energy

required to dissociate and form N-H and N-N bonds. The second mechanism tested for the release of C_3, SAC-Decomposition (Symmetric Alkaline Complete decomposition, Figure 5), did not involve diffusion and recombination but the formation of water with the OH$^-$ groups. Indeed, sodium hydroxide could interact and promote the reactivation of the C site to proceed with the dehydrogenation steps.
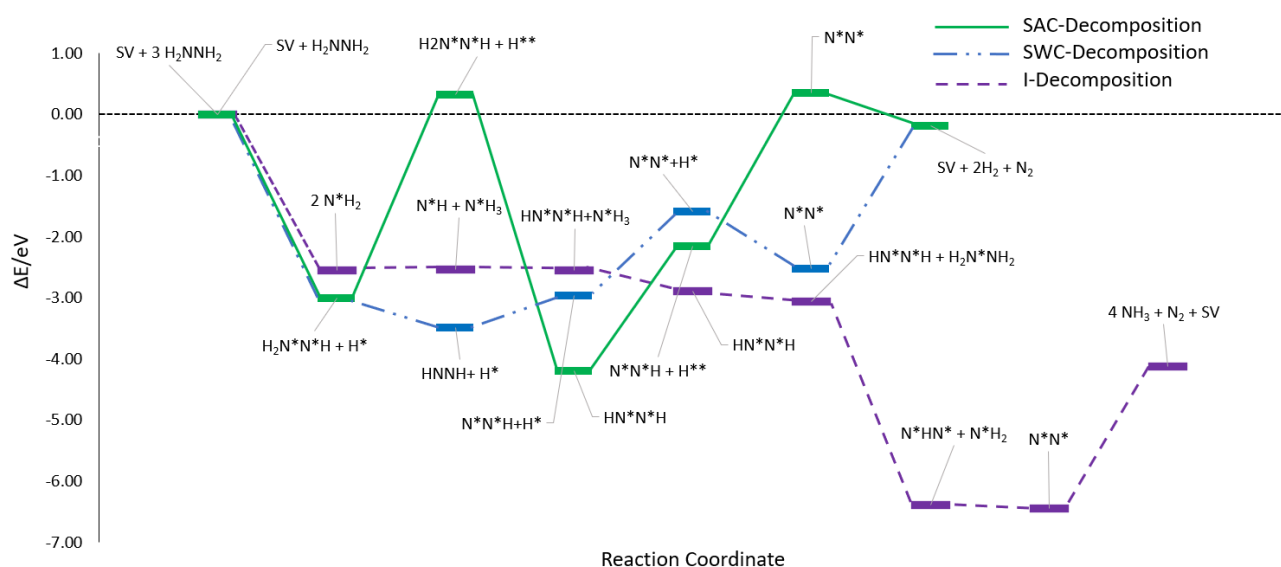

*Figure 5 Energy profiles for hydrazine decomposition pathways. Purple line indicates the incomplete decomposition pathway leading to NH$_3$(I-decomposition), blue and green lines indicate the two possibilities of symmetric dehydrogenation with NaOH and water (respectively SWC- and SAC- decomposition. In the SWC-Decomposition pathway H** indicates diffused atomic hydrogen species, a single * is used to indicate which atom is adsorbed on surface active sites.*

SWC H$_2$ production

The first dehydrogenation on cB-H structure, common to both SAC and SWC pathways, presented an increment in the N centres sp^3 character and the N-N bond stretches by about 0.03 Å, while the N-H stretching was negligible. The C_3-N and C_7-N bonds equilibrium lengths were not symmetric and differed by 0.058 Å. In addition, the initial SV site changed its structure to accommodate the adsorbed species (Figure 6a and **Error! Reference source not found.**a). In the following step along the SWC pathway, the adsorbed H$_2$N*N*H intermediate may take three different dehydrogenation pathways: two symmetric and one asymmetric (Figure 5). Among all symmetric decomposition pathways, SWC was the most favourable one, and for this reason, it will be the only one considered (Figure 5, SWC-decomposition). Upon diffusion on the co-adsorbed H (Figure 6b, E_R = 3.319 eV, the intermediate HNNH (Figure 6c) showed a N-N bond contraction of 0.037 Å and a reduction of the C_3-N and C_7-N bond lengths (0.094 Å and 0.005 Å, respectively). The superior stability of the adsorbed HN*N*H compared to the asymmetric counterpart, H$_2$N*N* ($\Delta E_{Asymm-Symm}$ = 0.739 eV) could be related to the higher symmetry of the structure. The energy needed to overcome the H$_2$ in-vacancy recombination energy leaded to an endothermic step (E_R = 1.066 eV). The subsequent step proceeded through the scission of another N-H bond (Figure 6d). The dehydrogenated N centre assumeed a sp^2 hybridization, i.e., planar configuration. The structure obtained was exceptionally exothermic due to an overall dangling carbons saturation (E_R of -3.625 eV). Nonetheless, the contribution of E_D (+3.48 eV) slightly increaseed the reaction energy. In the final structure (Figure 6e, E_R =+2.50 eV), N-N bond showed an additional contraction indicating an increasing sp hybridization, typical of molecular N$_2$, which spontaneously evolveed from the surface freeing the active site (E_R = -0.19 eV).
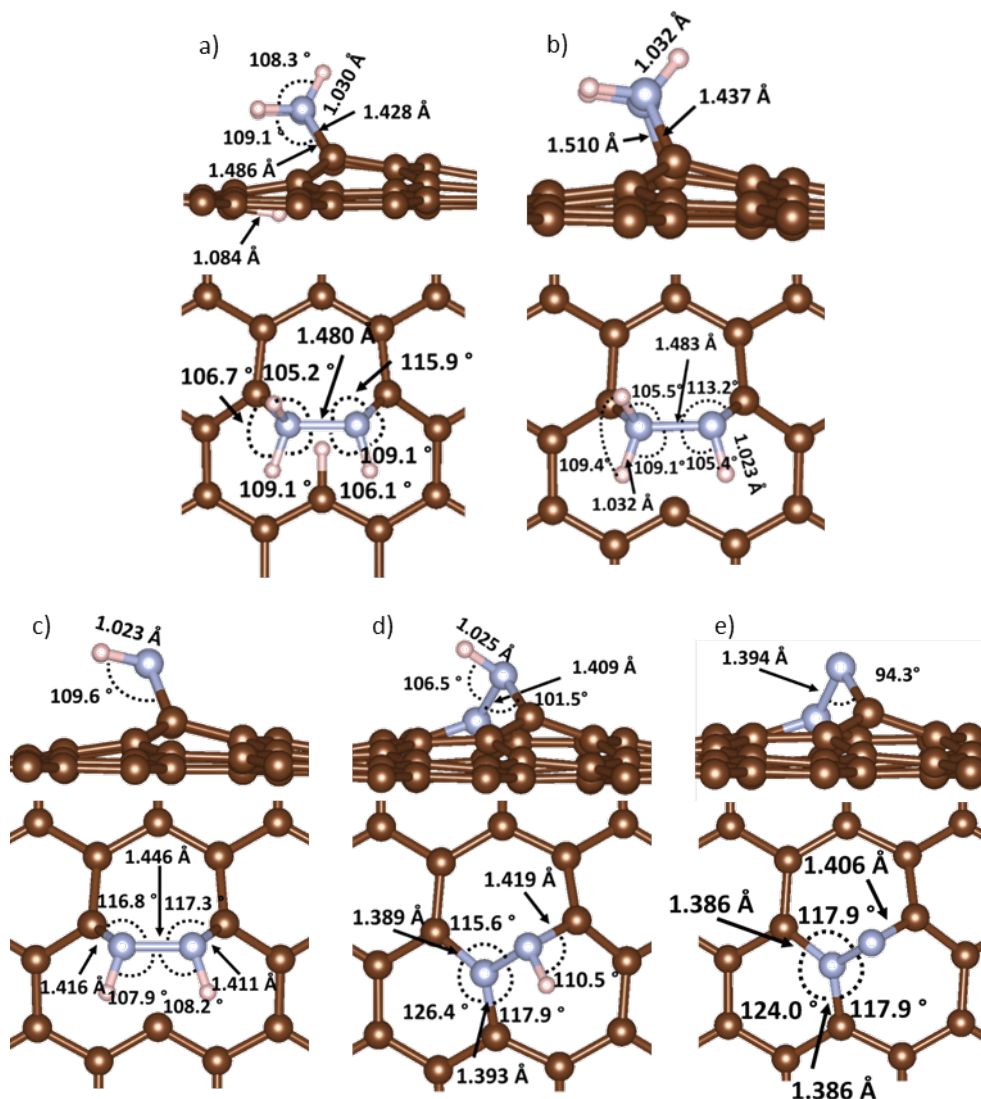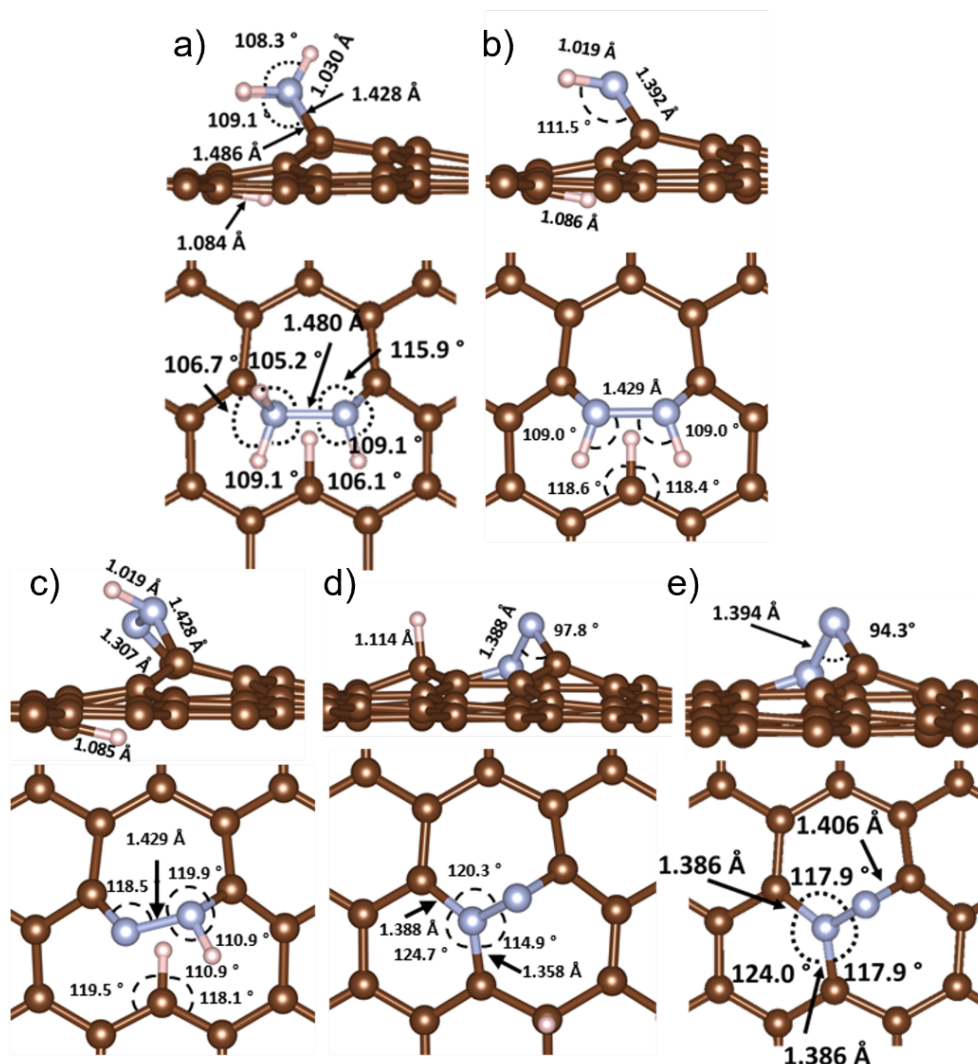
Figure 6: Top and side view of the most favourable hydrazine configurations for H₂ production in water: a) Dissociative adsorption step N*H₂N*H + H*, b) Hydrogen diffusion step N*H₂N*H + H**, c) second dehydrogenation step and H₂ evolution, N*HN* H, d) third dehydrogenation step with diffusion, N*N* H + H** and e) last dehydrogenation step, H₂ and N₂ evolution, N*N*. Inset, distances (Å) and angles (°) of interest. Carbon atoms are labelled in brown, nitrogen in blue and hydrogen in white.

SAC H2 production

The presence of NaOH as alkaline medium (SAC) leaded to a more favourable dehydrogenation pathway (Figure 5). **Error! Reference source not found.** shows the SAC-Decomposition mechanism where, in each step, the dangling bonds were completely saturated increasing its stability. The dissociative adsorption step (Figure 7a) was followed by a further hydrogen extraction (**Error! Reference source not found.**b, E_R = -0.491 eV) due to the interaction with OH⁻ ions, which presented an exothermic behaviour. Differently from the SWC, the formation of a C_3-H bond influenced both structures and energies ($\Delta E_{SWC-SAC}$ = 3.810 eV, Figure 6b and **Error! Reference source not found.**b). The N-H and C-N bonds were more contracted, in particular the C-N bonds respectively by 0.018 and 0.045 Å, while the N-H bonds by 0.004 and 0.013 Å. In the subsequent step (**Error! Reference source not found.**c, E_R = 0.525 eV), further dehydrogenation was performed with the *in-situ* evolution of a molecular hydrogen specie. The C-N bond related to the bare N centre contracted by 0.085 Å, while either N-N or N-H bonds did not show any variation. Moreover, it is possible to observe that the bare N centre tilted towards the C_3-H. Overall, the step is slightly endothermic, due to the breakage of the N-H bond. Subsequently (**Error! Reference source not found.**d), the bare N centre bonded to C_3 and a scission of the N-H bond occurred and the atomic H bonded to a non-active C atom (E_R = +1.377 eV). Indeed,

from **Error! Reference source not found.**d it is possible to observe that the structure was deformed in order to bond the H atoms. The structure of the last dehydrogenation step (**Error! Reference source not found.**e) was completely equivalent to the one described in the SWC mechanism (Figure 6e). Nonetheless, from the energetic point view, the difference was mainly related to H_2 evolution. Indeed, in the SWC mechanism it was necessary to overcome the energetic barrier deriving from the in-vacancy recombination of two diffused H atoms (E_R = 2.900 eV, Figure S6). Here, the hydrogen evolution did not require any recombination, leading to an exothermic step (E_R = -0.937 eV). In the last step, N_2 evolution was endothermic and required overcoming an energetic barrier of 2.328 eV.

Figure 7 Top and side view of the most favourable hydrazine configurations for H2 production in presence of aqueous NaOH: a) Dissociative adsorption step N*H2N*H + H*, b) Dehydrogenation step: N*HN*H + H*, c) second dehydrogenation step and H2 evolution, N*N* H + H*, d) third dehydrogenation step , N*N* + H* and e) last dehydrogenation step, H2 and N2 evolution, N*N*. Inset, distances (Å) and angles (°) of interest. Carbon atoms are labelled in brown, nitrogen in blue and hydrogen in white.

NH₃ production

The first step of NH_3 production (Figure 8a) involved the breakage of N-N bond upon adsorption, forming the cB-N structure (E_{ADS} = - 2.55 eV). The two adsorbed NH_2 lied on the dangling carbons with sp^3-like configuration. The following elementary step consisted in a hydrogen transfer, involving the two N^*H_2, followed by the NH_3 evolution. As can be seen from the structure in Figure 6b, the remaining N^*H tilted toward vacancy centre. A contraction of the free dangling carbons (C_3-$C_{3'}$) distance is then observed, leading to a slightly endothermic process (E_R = + 0.018 eV). To close the catalytic cycle, a subsequent hydrazine

adsorption bridging between the available active sites was considered (Figure 6c). The initial N*H took two hydrogen atoms from the second N_2H_4 in a concerted mechanism upon its adsorption, leading to the formation of HN*N*H + N*H$_3$. This step showed an overall exothermic energy (E_R = - 0.019 eV), along with the following NH$_3$ exothermic evolution process, leading HN*N*H on the SV (Figure 6d, E_R = - 0.35 eV). In the subsequent elementary step, a third hydrazine could exothermically co-adsorb on the under-coordinated carbon sites C_7 (E_R = -0.163 eV, Figure 8e). In this position, the third hydrazine molecule interacted with an H of the adsorbed HN*N*H yielding a NH$_3$ molecule (Figure 8e). The structure obtained is energetically favourable (E_R = -3.33 eV, Figure 8f) and the H-free N bridged between two carbon sites with a sp^2 hybridization. Instead, the C_7 atom was saturated connecting two N atom, showing a conventional sp^3 geometry. The interaction between N*H$_2$ and the H located on the bridged HN*N* leaded to the evolution of the last NH$_3$ (Figure 8f, E_R = -0.05 eV). The resulting N_2 was anchored on the carbon lattice (E_R = +2.32 eV) analogously to the SAC hydrogen production pathway.
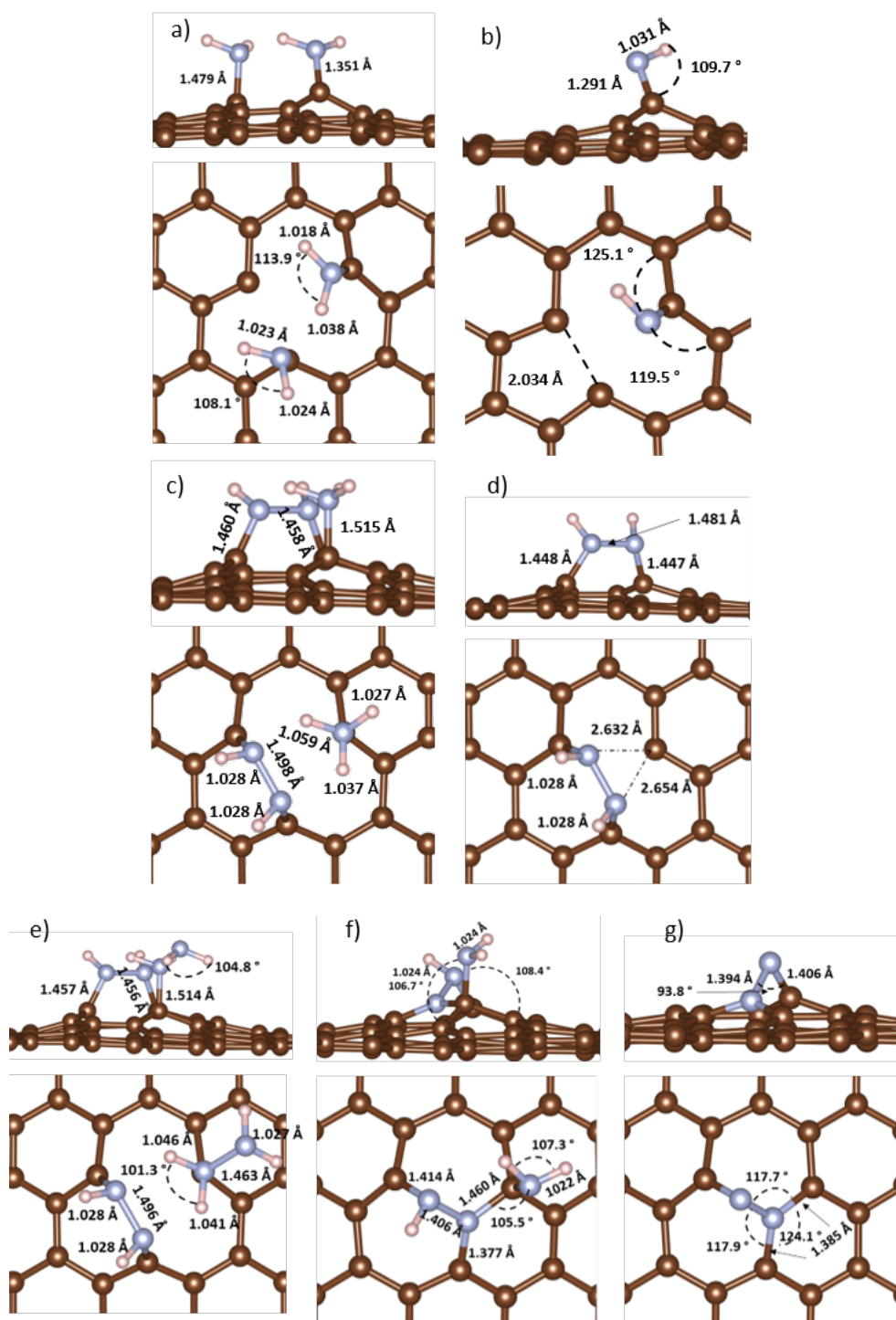
Figure 8 Top and side view of the most favourable Hydrazine configurations for NH₃ production: a) N-N bond breakage step, 2 N*H₂, b) First NH₃ evolution step, N*H, c) Second Hydrazine adsorption step, N*HN*H + N*H₃ , d) Second NH₃ evolution step, N*HN*H, e) Third Hydrazine linkage step, N*HN*H + N*H₂NH₂, f) Third NH₃ evolution step, N*HN* + N*H₂ and g) Fourth NH₃ and N₂ evolution step, N*N*. Inset, distances (Å) and angles (°) of interest. Carbon atom is labelled in brown, nitrogen in blue and hydrogen in white.

CONCLUSIONS

In this study, different metal-free carbonaceous materials, i.e. CNFs PS, CNFs HHT and graphite were tested in hydrazine hydrate decomposition reaction for the first time. In addition, a systematic density functional

theory (DFT) study on N_2H_4 adsorption and decomposition mechanism was then employed to understand the role of the defects paving the pathway to the development of new and efficient carbocatalysts to be used in this reaction. A conversion of 94 %, 71 % and 65 % was observed after 6 h of reaction for CNFs PS, CNFs HHT and graphite, respectively. For the best of our knowledge, this is the first work reported in literature which shows the ability of metal-free carbonaceous materials to decompose hydrazine hydrate. Moreover, a selectivity for H_2 of the 89 % at 97 % of conversion was found testing CNFs-PS. The materials were also analysed using ICP and Raman spectroscopy. A correlation between the numbers of defects present in the catalysts and the initial activity of the hydrazine decomposition reaction was found. In particular, initial activity increases increasing the number of defects, i.e. CNFs-PS > CNFs-HHT > graphite. Correlating the I_D/I_G ratio obtained by Raman spectroscopy and the initial activity, a linear correlation was found ($R^2 = 0.981$). In addition, CNFs PS were also tested in absence of alkaline medium to understand the effect of NaOH. The catalyst showed a conversion (15 % conversion at 4 h) lower than in presence of NaOH (94 % conversion at 4 h

In order to understand the effect of the defects on the decomposition of hydrazine, different surfaces were modelled using DFT calculation, i.e. pristine graphene, single and double vacancies, and different Stone–Wales defects. According to our previous studies, only SV showed an exothermic adsorption energy to our substrate, indicating that it is the only defect which participates in the reaction. Two symmetrical and one asymmetrical dehydrogenation pathways were found, but only the most favourable (symmetric hydrazine dehydrogenation) was considered in our discussion. On the most stable hydrogen production pathway, the effect of the alkaline medium was elucidated through calculations concerning the diffusion and recombination of atomic hydrogen. Indeed, the presence of NaOH helps extracting H species without additional energetic barriers, as opposed to the calculations performed in polarizable continuum medium. In addition, an incomplete decomposition pathway forming N_2 and NH_3 was studied and compared with the dehydrogenation one. Considering the initial dissociative adsorption, the first step of the dehydrogenation pathway is the more favourable (dissociation of the N-H bond, -3.00 eV) than the scission of the N-N bond (-2.55 eV) which lead to NH_3 as product. This first reaction step is crucial to define the reaction mechanisms and the computational results fully agree with the ones obtained in the experiments. Moreover, comparing two different hydrogen production pathways (with and without diffusion and recombination), we confirmed that the presence of sodium hydroxide in the experimental reaction environment can modify the energy gap between the two pathways, leading to a selectivity to H_2 near 90 %. Overall, this work provides a complete insight of hydrazine decomposition over intrinsic elementary defects of metal-free carbonaceous catalysts. Finally, these results can be used as a raw model for the synthesis of carbocatalysts with enhanced features for the liquid phase hydrazine decomposition reaction, focusing on widening the ΔE_{NN-NH} energy gap.

REFERENCES

[1]   T.N. Veziroğlu, S. Şahin, 21st Century's energy: Hydrogen energy system, Energy Convers. Manag. 49 (2008) 1820–1831. https://doi.org/10.1016/j.enconman.2007.08.015.

[2]   P. Nikolaidis, A. Poullikkas, A comparative overview of hydrogen production processes, Renew. Sustain. Energy Rev. 67 (2017) 597–611. https://doi.org/10.1016/j.rser.2016.09.044.

[3]   M.Z. Chen W, L Z ouyang, J W Liu, X D Yao, H Wang, Z W Liu, Hydrolysis and regeneration of sodium borohydride (NaBH4) – A combination of hydrogen production and storage, J. Power Sources. 359 (2017) 400–407. https://doi.org/10.1016/j.jpowsour.2017.05.075.

[4]   I. Shown, A. Ganguly, L.C. Chen, K.H. Chen, Conducting polymer-based flexible supercapacitor, Energy Sci. Eng. 3 (2015) 1–25. https://doi.org/10.1002/ese3.50.

[5]   K. Sordakis, C. Tang, L.K. Vogt, H. Junge, P.J. Dyson, M. Beller, G. Laurenczy, Homogeneous Catalysis for Sustainable Hydrogen Storage in Formic Acid and Alcohols, Chem. Rev. 118 (2018) 372–433. https://doi.org/10.1021/acs.chemrev.7b00182.

[6]   H. jin Jeon, Y.M. Chung, Hydrogen production from formic acid dehydrogenation over Pd/C catalysts: Effect of metal and support

properties on the catalytic performance, Appl. Catal. B Environ. 210 (2017) 212–222. https://doi.org/10.1016/j.apcatb.2017.03.070.

[7]   M. Yadav, Q. Xu, Liquid-phase chemical hydrogen storage materials, Energy Environ. Sci. 5 (2012) 9698–9725. https://doi.org/10.1039/c2ee22937d.

[8]   S.K. Singh, Q. Xu, Complete conversion of hydrous hydrazine to hydrogen at room temperature for chemical hydrogen storage, J. Am. Chem. Soc. 131 (2009) 18032–18033. https://doi.org/10.1021/ja908037t.

[9]   S.K. Singh, Z. Lu, Q. Xu, Temperature-Induced Enhancement of Catalytic Performance in Selective Hydrogen Generation from Hydrous Hydrazine with Ni-Based Nanocatalysts for Chemical Hydrogen Storage, Eur. J. Inorg. Chem. 2011 (2011) 2232–2237. https://doi.org/10.1002/ejic.201100083.

[10]   S.K. Singh, X.-B. Zhang, Q. Xu, Room-Temperature Hydrogen Generation from Hydrous Hydrazine for Chemical Hydrogen Storage, J. Am. Chem. Soc. 131 (2009) 9894–9895. https://doi.org/10.1021/ja903869y.

[11]   S.K. Singh, A.K. Singh, K. Aranishi, Q. Xu, Noble-metal-free bimetallic nanoparticle-catalyzed selective hydrogen generation from hydrous hydrazine for chemical hydrogen storage, J. Am. Chem. Soc. 133 (2011) 19638–19641. https://doi.org/10.1021/ja208475y.

[12]   R. Lan, J.T.S. Irvine, S. Tao, Ammonia and related chemicals as potential indirect hydrogen storage materials, Int. J. Hydrogen Energy. 37 (2012) 1482–1494. https://doi.org/10.1016/j.ijhydene.2011.10.004.

[13]   L. Giorgi, A. Pozio, C. Bracchini, R. Giorgi, S. Turtù, H2 and H2/CO oxidation mechanism on Pt/C, Ru/C and Pt–Ru/C electrocatalysts, J. Appl. Electrochem. 31 (2001) 325–334. https://doi.org/10.1023/A:1017595920726.

[14]   M. Pravica, L. Bai, Y. Liu, Hydrazine at high pressure, Chem. Phys. Lett. 555 (2013) 115–118. https://doi.org/https://doi.org/10.1016/j.cplett.2012.10.079.

[15]   A.S. Shteinberg, High-Temperature Decomposition and Thermal Explosion of Liquid Propellant Components: Hydrogen Peroxide and Hydrazine BT - Fast Reactions in Energetic Materials: High-Temperature Decomposition of Rocket Propellants and Explosives, in: A.S. Shteinberg (Ed.), Springer Berlin Heidelberg, Berlin, Heidelberg, 2008: pp. 173–198. https://doi.org/10.1007/978-3-540-78861-4_11.

[16]   J.K. Norskov, C.H. Christensen, Toward Efficient Hydrogen Production at Surfaces, Science (80-.). 312 (2006) 1322 LP – 1323. https://doi.org/10.1126/science.1127180.

[17]   S.E. Wood, J.T. Bryant, Decomposition of Hydrazine on Shell 405 Catalyst at High Presure, Prod. R&D. 12 (1973) 117–122. https://doi.org/10.1021/i360046a004.

[18]   T.G. Soares Neto, A.J.G. Cobo, G.M. Cruz, Textural properties evolution of Ir and Ru supported on alumina catalysts during hydrazine decomposition in satellite thruster, Appl. Catal. A Gen. 250 (2003) 331–340. https://doi.org/https://doi.org/10.1016/S0926-860X(03)00301-6.

[19]   J.P. Contour, G. Pannetier, Hydrazine decomposition over a supported iridium catalyst, J. Catal. 24 (1972) 434–445.

[20]   R. Maurel, J.C. Menezo, Catalytic decomposition of 15N-labeled hydrazine on alumina-supported metals, J. Catal. 51 (1978) 293–295.

[21]   P.-X. Zhang, Y.-G. Wang, Y.-Q. Huang, T. Zhang, G.-S. Wu, J. Li, Density functional theory investigations on the catalytic mechanisms of hydrazine decompositions on Ir (1 1 1), Catal. Today. 165 (2011) 80–88.

[22]   A.K. Singh, M. Yadav, K. Aranishi, Q. Xu, Temperature-induced selectivity enhancement in hydrogen generation from Rh–Ni nanoparticle-catalyzed decomposition of hydrous hydrazine, Int. J. Hydrogen Energy. 37 (2012) 18915–18919. https://doi.org/10.1016/j.ijhydene.2012.09.104.

[23]   L. Zhou, X. Luo, L. Xu, C. Wan, M. Ye, Pt-ni nanoalloys for H2 generation from hydrous hydrazine, Catalysts. 10 (2020). https://doi.org/10.3390/catal10080930.

[24]   L. He, B. Liang, L. Li, X. Yang, Y. Huang, A. Wang, X. Wang, T. Zhang, Cerium-oxide-modified nickel as a non-noble metal catalyst for selective decomposition of hydrous hydrazine to hydrogen, Acs Catal. 5 (2015) 1623–1628.

[25]   M. Zheng, R. Cheng, X. Chen, N. Li, L. Li, X. Wang, T. Zhang, A novel approach for CO-free H2 production via catalytic decomposition of hydrazine, Int. J. Hydrogen Energy. 30 (2005) 1081–1089. https://doi.org/10.1016/j.ijhydene.2004.09.014.

[26]   S.K. Singh, Q. Xu, Nanocatalysts for hydrogen generation from hydrazine, Catal. Sci. Technol. 3 (2013) 1889–1900. https://doi.org/10.1039/c3cy00101f.

[27]   Y. Cheng, X. Wu, H. Xu, Catalytic decomposition of hydrous hydrazine for hydrogen production, Sustain. Energy Fuels. 3 (2019) 343–365. https://doi.org/10.1039/c8se00538a.

[28]   Z. Zhang, S. Zhang, Q. Yao, X. Chen, Z.-H. Lu, Controlled Synthesis of MOF-Encapsulated NiPt Nanoparticles toward Efficient and Complete Hydrogen Evolution from Hydrazine Borane and Hydrazine, Inorg. Chem. 56 (2017) 11938–11945. https://doi.org/10.1021/acs.inorgchem.7b01910.

[29]   S.J. Cho, J. Lee, Y.S. Lee, D.P. Kim, Characterization of Iridium Catalyst for Decomposition of Hydrazine Hydrate for Hydrogen Generation,

Catal. Letters. 109 (2006) 181–186. https://doi.org/10.1007/s10562-006-0081-3.

[30]   H.-L. Jiang, S.K. Singh, J.-M. Yan, X.-B. Zhang, Q. Xu, Liquid-Phase Chemical Hydrogen Storage: Catalytic Hydrogen Generation under Ambient Conditions, ChemSusChem. 3 (2010) 541–549. https://doi.org/https://doi.org/10.1002/cssc.201000023.

[31]   P.Z. Li, Q. Xu, Metal-nanoparticle catalyzed hydrogen generation from liquid-phase chemical hydrogen storage materials, J. Chinese Chem. Soc. 59 (2012) 1181–1189. https://doi.org/10.1002/jccs.201200033.

[32]   Y.-P. Qiu, H. Yin, H. Dai, L.-Y. Gan, H.-B. Dai, P. Wang, Tuning the Surface Composition of Ni/meso-CeO2 with Iridium as an Efficient Catalyst for Hydrogen Generation from Hydrous Hydrazine, Chem. – A Eur. J. 24 (2018) 4902–4908. https://doi.org/https://doi.org/10.1002/chem.201705923.

[33]   Y.-Y. Jiang, H.-B. Dai, Y.-J. Zhong, D.-M. Chen, P. Wang, Complete and Rapid Conversion of Hydrazine Monohydrate to Hydrogen over Supported Ni–Pt Nanoparticles on Mesoporous Ceria for Chemical Hydrogen Storage, Chem. – A Eur. J. 21 (2015) 15439–15445. https://doi.org/https://doi.org/10.1002/chem.201502421.

[34]   P. Zhao, N. Cao, J. Su, W. Luo, G. Cheng, NiIr Nanoparticles Immobilized on the Pores of MIL-101 as Highly Efficient Catalyst toward Hydrogen Generation from Hydrous Hydrazine, ACS Sustain. Chem. Eng. 3 (2015) 1086–1093. https://doi.org/10.1021/acssuschemeng.5b00009.

[35]   Y.B. Jang, T.H. Kim, M.H. Sun, J. Lee, S.J. Cho, Preparation of iridium catalyst and its catalytic activity over hydrazine hydrate decomposition for hydrogen production and storage, Catal. Today. 146 (2009) 196–201.

[36]   X. Du, P. Cai, W. Luo, G. Cheng, Facile synthesis of P-doped Rh nanoparticles with superior catalytic activity toward dehydrogenation of hydrous hydrazine, Int. J. Hydrogen Energy. 42 (2017) 6137–6143. https://doi.org/https://doi.org/10.1016/j.ijhydene.2016.12.049.

[37]   N. Cao, L. Yang, H. Dai, T. Liu, J. Su, X. Wu, W. Luo, G. Cheng, Immobilization of Ultrafine Bimetallic Ni–Pt Nanoparticles Inside the Pores of Metal–Organic Frameworks as Efficient Catalysts for Dehydrogenation of Alkaline Solution of Hydrazine, Inorg. Chem. 53 (2014) 10122–10128. https://doi.org/10.1021/ic5010352.

[38]   R. Jiang, X. Qu, F. Zeng, Q. Li, X. Zheng, Z. Xu, J. Peng, MOF-74-immobilized ternary RhNiP nanoparticles as highly efficient hydrous hydrazine dehydrogenation catalysts in alkaline solutions, Int. J. Hydrogen Energy. 44 (2019) 6383–6391. https://doi.org/https://doi.org/10.1016/j.ijhydene.2019.01.117.

[39]   L. He, B. Liang, Y. Huang, T. Zhang, Design strategies of highly selective nickel catalysts for H2 production via hydrous hydrazine decomposition: a review, Natl. Sci. Rev. 5 (2018) 356–364. https://doi.org/10.1093/nsr/nwx123.

[40]   L. He, Y. Huang, X.Y. Liu, L. Li, A. Wang, X. Wang, C.-Y. Mou, T. Zhang, Structural and catalytic properties of supported Ni–Ir alloy catalysts for H2 generation via hydrous hydrazine decomposition, Appl. Catal. B Environ. 147 (2014) 779–788.

[41]   Y. Qiu, H. Yin, H. Dai, L. Gan, H. Dai, P. Wang, Tuning the Surface Composition of Ni/meso-CeO2 with Iridium as an Efficient Catalyst for Hydrogen Generation from Hydrous Hydrazine, Chem. Eur. J. 24 (2018) 4902–4908.

[42]   J. Chen, Q. Yao, J. Zhu, X. Chen, Z.-H. Lu, Rh–Ni nanoparticles immobilized on Ce (OH) CO3 nanorods as highly efficient catalysts for hydrogen generation from alkaline solution of hydrazine, Int. J. Hydrogen Energy. 41 (2016) 3946–3954.

[43]   Y. Jiang, H. Dai, Y. Zhong, D. Chen, P. Wang, Complete and rapid conversion of hydrazine monohydrate to hydrogen over supported Ni–Pt nanoparticles on mesoporous ceria for chemical hydrogen storage, Chem. Eur. J. 21 (2015) 15439–15445.

[44]   H. Wang, L. Wu, Y. Wang, X. Li, Y. Wang, Facile synthesis of Ni nanoparticles from triangular Ni (HCO3) 2 nanosheets as catalysts for hydrogen generation from hydrous hydrazine, Catal. Commun. 100 (2017) 33–37.

[45]   S.N. Oliaee, C. Zhang, S.Y. Hwang, H.M. Cheung, Z. Peng, Hydrogen production via hydrazine decomposition on model platinum-nickel nanocatalyst with a single (111) facet, J. Phys. Chem. C. 120 (2016) 9764–9772. https://doi.org/10.1021/acs.jpcc.6b00815.

[46]   J. Wang, X.-B. Zhang, Z.-L. Wang, L.-M. Wang, Y. Zhang, Rhodium–nickel nanoparticles grown on graphene as highly efficient catalyst for complete decomposition of hydrous hydrazine at room temperature for chemical hydrogen storage, Energy Environ. Sci. 5 (2012) 6885. https://doi.org/10.1039/c2ee03344e.

[47]   U. Sikander, S. Sufian, M.A. Salam, A review of hydrotalcite based catalysts for hydrogen production systems, Int. J. Hydrogen Energy. 42 (2017) 19851–19868. https://doi.org/10.1016/j.ijhydene.2017.06.089.

[48]   Z. Liu, J. Li, S. Xue, S. Zhou, K. Qu, Y. Li, W. Cai, Pt/Mo2C heteronanosheets for superior hydrogen evolution reaction, J. Energy Chem. 47 (2020) 317–323. https://doi.org/10.1016/j.jechem.2020.02.005.

[49]   C. Li, J.B. Baek, Recent Advances in Noble Metal (Pt, Ru, and Ir)-Based Electrocatalysts for Efficient Hydrogen Evolution Reaction, ACS Omega. 5 (2020) 31–40. https://doi.org/10.1021/acsomega.9b03550.

[50]   X. Zhou, Y. Huang, W. Xing, C. Liu, J. Liao, T. Lu, High-quality hydrogen from the catalyzed decomposition of formic acid by Pd-Au/C and Pd-Ag/C, Chem. Commun. (2008) 3540–3542. https://doi.org/10.1039/b803661f.

[51]   J.A. Herron, J. Scaranto, P. Ferrin, S. Li, M. Mavrikakis, Trends in formic acid decomposition on model transition metal surfaces: A density

functional theory study, ACS Catal. 4 (2014) 4434–4445. https://doi.org/10.1021/cs500737p.

[52]   N. Gupta, O. Khavryuchenko, A. Villa, D. Su, Metal-Free Oxidation of Glycerol over Nitrogen-Containing Carbon Nanotubes, ChemSusChem. 10 (2017) 3030–3034. https://doi.org/10.1002/cssc.201700940.

[53]   P. Veerakumar, P. Thanasekaran, T. Subburaj, K.-C. Lin, A Metal-Free Carbon-Based Catalyst: An Overview and Directions for Future Research, C. 4 (2018) 54. https://doi.org/10.3390/c4040054.

[54]   M.M. Titirici, M. Antonietti, Chemistry and materials options of sustainable carbon materials made by hydrothermal carbonization, Chem. Soc. Rev. 39 (2010) 103–116. https://doi.org/10.1039/b819318p.

[55]   G. Mestl, N.I. Maksimova, N. Keller, V. V. Roddatis, R. Schlögl, Carbon Nanofilaments in Heterogeneous Catalysis: An Industrial Application for New Carbon Materials?, Angew. Chemie - Int. Ed. 40 (2001) 2066–2068. https://doi.org/10.1002/1521-3773(20010601)40:11<2066::AID-ANIE2066>3.0.CO;2-I.

[56]   P.N. Optics, N. York, Surface-Modified Carbon Nanotubes, 322 (2008) 73–78.

[57]   J. Zhang, D.S. Su, R. Blume, R. Schlögl, R. Wang, X. Yang, A. Gajović, Surface chemistry and catalytic reactivity of a nanodiamond in the steam-free dehydrogenation of ethylbenzene, Angew. Chemie - Int. Ed. 49 (2010) 8640–8644. https://doi.org/10.1002/anie.201002869.

[58]   J.H. Yang, G. Sun, Y. Gao, H. Zhao, P. Tang, J. Tan, A.H. Lu, D. Ma, Direct catalytic oxidation of benzene to phenol over metal-free graphene-based catalyst, Energy Environ. Sci. 6 (2013) 793–798. https://doi.org/10.1039/c3ee23623d.

[59]   D.R. Dreyer, H.P. Jia, C.W. Bielawski, Graphene oxide: A convenient carbocatalyst for facilitating oxidation and hydration reactions, Angew. Chemie - Int. Ed. 49 (2010) 6813–6816. https://doi.org/10.1002/anie.201002160.

[60]   M.A. Patel, F. Luo, M.R. Khoshi, E. Rabie, Q. Zhang, C.R. Flach, R. Mendelsohn, E. Garfunkel, M. Szostak, H. He, P-Doped Porous Carbon as Metal Free Catalysts for Selective Aerobic Oxidation with an Unexpected Mechanism, ACS Nano. 10 (2016) 2305–2315. https://doi.org/10.1021/acsnano.5b07054.

[61]   A. Primo, F. Neatu, M. Florea, V. Parvulescu, H. Garcia, Graphenes in the absence of metals as carbocatalysts for selective acetylene hydrogenation and alkene hydrogenation, Nat. Commun. 5 (2014) 1–9. https://doi.org/10.1038/ncomms6291.

[62]   Y. Gao, D. Ma, C. Wang, J. Guan, X. Bao, Reduced graphene oxide as a catalyst for hydrogenation of nitrobenzene at room temperature, Chem. Commun. 47 (2011) 2432–2434. https://doi.org/10.1039/c0cc04420b.

[63]   I. Barlocco, S. Capelli, X. Lu, S. Tumiati, N. Dimitratos, A. Roldan, A. Villa, Role of defects in carbon materials during metal-free formic acid dehydrogenation, Nanoscale. (2020) 22768–22777. https://doi.org/10.1039/d0nr05774f.

[64]   X. Lu, A. Roldan, Are Carbon-Based Materials Good Supports for the Catalytic Reforming of Ammonia?, J. Phys. Chem. C. (2021). https://doi.org/10.1021/acs.jpcc.1c03996.

[65]   F. Zheng, H. Dong, Y. Ji, Y. Li, Adsorption and catalytic decomposition of hydrazine on metal-free SiC 3 siligraphene, Appl. Surf. Sci. 469 (2019) 316–324. https://doi.org/10.1016/j.apsusc.2018.11.002.

[66]   C. Gojon, B. Dureault, Spectrophotometric study of the reaction between hydrazine and p.dimethylaminobenzaldehyde, J. Nucl. Sci. Technol. 33 (1996) 731–735. https://doi.org/10.1080/18811248.1996.9731989.

[67]   W.D. Basson, J.F. Van Staden, Low-level determination of hydrazine in boiler feed water with an unsegmented high-speed continuous-flow system, Analyst. 103 (1978) 998–1001. https://doi.org/10.1039/AN9780300998.

[68]   G. Kresse, J. Furthmüller, Efficient iterative schemes for ab initio total-energy calculations using a plane-wave basis set, Phys. Rev. B - Condens. Matter Mater. Phys. 54 (1996) 11169–11186. https://doi.org/10.1103/PhysRevB.54.11169.

[69]   G. Kresse, Ab initio molecular dynamics for liquid metals, J. Non. Cryst. Solids. 192–193 (1995) 222–229. https://doi.org/10.1016/0022-3093(95)00355-X.

[70]   B. Hammer, L.B. Hansen, J.K. Nørskov, Improved adsorption energetics within density-functional theory using revised Perdew-Burke-Ernzerhof functionals, Phys. Rev. B. 59 (1999) 7413–7421. https://doi.org/10.1103/PhysRevB.59.7413.

[71]   N.D. Mermin, Thermal properties of the inhomogeneous electron gas, Phys. Rev. 137 (1965) 1–3. https://doi.org/10.1103/PhysRev.137.A1441.

[72]   R. Sure, J. Antony, S. Grimme, Blind prediction of binding affinities for charged supramolecular host–guest systems: achievements and shortcomings of DFT-D3, J. Phys. Chem. B. 118 (2014) 3431–3440.

[73]   S. Ehrlich, J. Moellmann, W. Reckien, T. Bredow, S. Grimme, System-Dependent Dispersion Coefficients for the DFT-D3 Treatment of Adsorption Processes on Ionic Surfaces, ChemPhysChem. 12 (2011) 3414–3420.

[74]   H. Fang, A. Roldan, C. Tian, Y. Zheng, X. Duan, K. Chen, L. Ye, S. Leoni, Y. Yuan, Structural tuning and catalysis of tungsten carbides for the regioselective cleavage of C–O bonds, J. Catal. 369 (2019) 283–295. https://doi.org/10.1016/j.jcat.2018.11.020.

[75] X. Lu, S. Francis, D. Motta, N. Dimitratos, A. Roldan, Mechanistic study of hydrazine decomposition on Ir(111), Phys. Chem. Chem. Phys. 22 (2020) 3883–3896. https://doi.org/10.1039/c9cp06525c.

[76] E. Nowicka, S. Althahban, T.D. Leah, G. Shaw, D. Morgan, C.J. Kiely, A. Roldan, G.J. Hutchings, Benzyl alcohol oxidation with Pd-Zn/TiO2: computational and experimental studies, Sci. Technol. Adv. Mater. 20 (2019) 367–378. https://doi.org/10.1080/14686996.2019.1598237.

[77] M.G. Quesne, A. Roldan, N.H. De Leeuw, C.R.A. Catlow, Carbon dioxide and water co-adsorption on the low-index surfaces of TiC, VC, ZrC and NbC: A DFT study, Phys. Chem. Chem. Phys. 21 (2019) 10750–10760. https://doi.org/10.1039/c9cp00924h.

[78] R. Sundararaman, K. Schwarz, Evaluating continuum solvation models for the electrode-electrolyte interface: Challenges and strategies for improvement, J. Chem. Phys. 146 (2017). https://doi.org/10.1063/1.4976971.

[79] K. Mathew, R. Sundararaman, K. Letchworth-Weaver, T.A. Arias, R.G. Hennig, Implicit solvation model for density-functional study of nanocrystal surfaces and reaction pathways, J. Chem. Phys. 140 (2014). https://doi.org/10.1063/1.4865107.

[80] J.D. Pack, H.J. Monkhorst, "special points for Brillouin-zone integrations"-a reply, Phys. Rev. B. 16 (1977) 1748–1749. https://doi.org/10.1103/PhysRevB.16.1748.

[81] Y.W. Tan, H.L. Stormer, P. Kim, K.S. Novoselov, M.L. Cohen, S.G. Louie, X. Wang, L. Zhang, S. Lee, H. Dai, Y. Kobayashi, K. Fukui, M. Fujita, G. Dresselhaus, M.S. Dresselhaus, M.A. Pimenta, B.R.A. Neves, A. Jorio, Y. Zhang, M. Mailman, P.M. Ajayan, S.K. Nayak, C.H. Park, Y.W. Son, S.P. Lu, S. Piscanec, A.C. Ferrari, G. Dobrik, P. Lambin, A. Oberlin, T. Solid, K. Suenaga, S. Iijima, P. Hermet, V. Meunier, L. Henrard, D. Gunlycke, C.T. White, S. Chen, B.I. Yakobson, S. Gradecak, Graphene at the Edge: Stability and Dynamics, Science (80-.). 323 (2009) 1705–1708.

[82] G. Henkelman, A. Arnaldsson, H. Jónsson, A fast and robust algorithm for Bader decomposition of charge density, Comput. Mater. Sci. 36 (2006) 354–360. https://doi.org/10.1016/j.commatsci.2005.04.010.

[83] M. Yu, D.R. Trinkle, Accurate and efficient algorithm for Bader charge integration, J. Chem. Phys. 134 (2011) 1–8. https://doi.org/10.1063/1.3553716.

[84] P.L.A. Popelier, On the full topology of the Laplacian of the electron density, Coord. Chem. Rev. 197 (2000) 169–189. https://doi.org/10.1016/s0010-8545(99)00189-7.

[85] D. Vega, D. Almeida, AIM-UC: An application for QTAIM analysis, J. Comput. Methods Sci. Eng. 14 (2014) 131–136.

[86] V.A. Borodin, T.T. Vehviläinen, M.G. Ganchenkova, R.M. Nieminen, Hydrogen transport on graphene: Competition of mobility and desorption, Phys. Rev. B - Condens. Matter Mater. Phys. 84 (2011) 1–15. https://doi.org/10.1103/PhysRevB.84.075486.

[87] F. Tuinstra, J.L. Koenig, Raman Spectrum of Graphite, J. Chem. Phys. 53 (1970) 1126–1130. https://doi.org/10.1063/1.1674108.

[88] C.R. Wick, T. Clark, On bond-critical points in QTAIM and weak interactions, J. Mol. Model. 24 (2018) 1–9. https://doi.org/10.1007/s00894-018-3684-x.

[89] L. Ma, J.M. Zhang, K.W. Xu, V. Ji, A first-principles study on gas sensing properties of graphene and Pd-doped graphene, Appl. Surf. Sci. 343 (2015) 121–127. https://doi.org/10.1016/j.apsusc.2015.03.068.

[90] X.Y. Liu, J.M. Zhang, K.W. Xu, V. Ji, Improving SO 2 gas sensing properties of graphene by introducing dopant and defect: A first-principles study, Appl. Surf. Sci. 313 (2014) 405–410. https://doi.org/10.1016/j.apsusc.2014.05.223.

[91] S. Yang, Z. Lan, H. Xu, G. Lei, W. Xie, Q. Gu, A First-Principles Study on Hydrogen Sensing Properties of Pristine and Mo-Doped Graphene, J. Nanotechnol. 2018 (2018). https://doi.org/10.1155/2018/2031805.

[92] D.C. de Oliveira, W.O. Silva, M. Chatenet, F.H.B. Lima, NiOx-Pt/C nanocomposites: Highly active electrocatalysts for the electrochemical oxidation of hydrazine, Appl. Catal. B Environ. 201 (2017) 22–28. https://doi.org/https://doi.org/10.1016/j.apcatb.2016.08.007.

[93] B. Luo, T. Wu, L. Zhang, F. Diao, Y. Zhang, L. Ci, J. Ulstrup, J. Zhang, P. Si, Monometallic nanoporous nickel with high catalytic performance towards hydrazine electro-conversion and its DFT calculations, Electrochim. Acta. 317 (2019) 449–458. https://doi.org/https://doi.org/10.1016/j.electacta.2019.05.123.

[94] X. Lu, S. Francis, D. Motta, N. Dimitratos, A. Roldan, Mechanistic study of hydrazine decomposition on Ir (111), Phys. Chem. Chem. Phys. 22 (2020) 3883–3896.

[95] S.S. Tafreshi, A. Roldan, N.H. de Leeuw, Density functional theory calculations of the hydrazine decomposition mechanism on the planar and stepped Cu (111) surfaces, Phys. Chem. Chem. Phys. 17 (2015) 21533–21546.

[96] M.K. Agusta, H. Kasai, First principles investigations of hydrazine adsorption conformations on Ni (111) surface, Surf. Sci. 606 (2012) 766–771.

[97] H. Yin, Y.-P. Qiu, H. Dai, L.-Y. Gan, H.-B. Dai, P. Wang, Understanding of selective H2 generation from hydrazine decomposition on Ni (111) surface, J. Phys. Chem. C. 122 (2018) 5443–5451.

[98] M.K. Agusta, M. David, H. Nakanishi, H. Kasai, Hydrazine (N2H4) adsorption on Ni (1 0 0)–density functional theory investigation, Surf. Sci.

604 (2010) 245–251.

[99]   M.K. Agusta, W.A. Diño, M. David, H. Nakanishi, H. Kasai, Theoretical study of hydrazine adsorption on Pt (111): Anti or cis?, Surf. Sci. 605 (2011) 1347–1353.

[100]   D. Zhao, D. Lü, Y. Zang, X. Zhao, Spillover in heterogeneous catalysis, Prog. Chem. 9 (1997) 759–788.

[101]   C.P. Herrero, R. Ramírez, Vibrational properties and diffusion of hydrogen on graphene, Phys. Rev. B - Condens. Matter Mater. Phys. 79 (2009) 1–8. https://doi.org/10.1103/PhysRevB.79.115429.

[102]   Y. Lei, S.A. Shevlin, W. Zhu, Z.X. Guo, Hydrogen-induced magnetization and tunable hydrogen storage in graphitic structures, Phys. Rev. B - Condens. Matter Mater. Phys. 77 (2008) 1–8. https://doi.org/10.1103/PhysRevB.77.134114.

[103]   L. Chen, A.C. Cooper, G.P. Pez, H. Cheng, Mechanistic study on hydrogen spillover onto graphitic carbon materials, J. Phys. Chem. C. 111 (2007) 18995–19000. https://doi.org/10.1021/jp074920g.

[104]   E. Skúlason, V. Tripkovic, M.E. Björketun, S. Gudmundsdóttir, G. Karlberg, J. Rossmeisl, T. Bligaard, H. Jónsson, J.K. Nørskov, Modeling the electrochemical hydrogen oxidation and evolution reactions on the basis of density functional theory calculations, J. Phys. Chem. C. 114 (2010) 18182–18197. https://doi.org/10.1021/jp1048887.

[105]   L. Liu, M. Qing, Y. Wang, S. Chen, Defects in Graphene: Generation, Healing, and Their Effects on the Properties of Graphene: A Review, J. Mater. Sci. Technol. 31 (2015) 599–606. https://doi.org/https://doi.org/10.1016/j.jmst.2014.11.019.

[106]   F. Banhart, J. Kotakoski, A. V. Krasheninnikov, Structural defects in graphene, ACS Nano. 5 (2011) 26–41. https://doi.org/10.1021/nn102598m.

[107]   S.S. Tafreshi, A. Roldan, N.H. De Leeuw, Density Functional Theory Study of the Adsorption of Hydrazine on the Perfect and Defective Copper (100), (110), and (111) Surfaces, J. Phys. Chem. C. 118 (2014) 26103–26114. https://doi.org/10.1021/jp5078664.